RSC Advances




ROYAL SOCIETY OF CHEMISTRY

www.rsc.org/advances

RSC Advances

RSCPublishing

PAPER

Cite this: DOI: 10.1039/x0xx00000x
Received 00th December 2015,
Accepted 00th February 2016
DOI: 10.1039/x0xx00000x
www.rsc.org/

# Novel synthesis of bismuth oxyiodide/graphitic carbon nitride nanocomposite with enhanced visible-light photocatalytic activity†

Shang-Yi Chou,[a] Chiing-Chang Chen,[a]* Yong-Ming Dai,[a] Jia-Hao Lin[a] and Wenlian William Lee[b, c]*

The first systematic synthetic study of bismuth oxyiodide/graphitic carbon nitride ($BiO_xI_y/g\text{-}C_3N_4$) nanocomposite preparation using controlled hydrothermal method is reported. The structure and morphology of $BiO_xI_y/g\text{-}C_3N_4$ photocatalysts are characterized by XRD, TEM, FT-IR, HR-XPS, FE-SEM-EDS, UV-vis-DRS and BET. The photodragrdation activities are evaluated against the decolorization of crystal violet (CV) in aqueous solution under visible light illumination. In particular, the catalytic performance illustrates the best reaction rate constant being 0.170 $h^{-1}$ once using $Bi_7O_9I_3/Bi_5O_7I/g\text{-}C_3N_4$ composite as the photocatalyst; which is 5, 4, and 1.5 times higher than the reaction rate constant of BiOI, $g\text{-}C_3N_4$, and $Bi_7O_9I_3/Bi_5O_7I$, as photocatalysts, respectively. From the quenching effects of different scavengers, the EPR results demonstrate that the reactive $O_2^{\bullet-}$ play the major roles and $h^+$ and $^{\bullet}OH$ plays the minor role in the CV degradation. The probable photodegradation mechanisms are proposed and discussed in this research. This work is useful for the synthesis of $BiO_xI_y/g\text{-}C_3N_4$ and the photocatalytic degradation of the CV at future applications to environmental pollution and control.

## 1. Introduction

The elimination of toxic chemicals from wastewater has become one of the most crucial aspects of contemporary pollution-control methods because of the deteriorating effects of such chemicals on living beings and the environment. Cationic triarylmethane (TPM) dyes were found the use as colorants in industry and as antimicrobial agents.[1] Recent reports showed that they might further supply as targetable sensitizers in the photo-destruction of specific cellular components (or cells).[2] The binding of CV to DNA was probably ionic, as opposed to intercalative, and it persisted so stably bound to double-stranded DNA that, with its conversion to the colorless carbinol form, it was used for assessing the binding of other molecules to DNA.[3] However, great troubles were arisen about the thyroid peroxidase-catalyzed oxidation of the triarylmethane class of dyes because the reactions might produce various *N*-de-alkylated primary and secondary aromatic amines, with the structures similar to aromatic amine carcinogens.[4]

Heterogeneous photocatalysis for solar energy conversion and environmental remediationhas fomented extensive interests in the past decade. For the practical applications of photocatalysis, an environmentally powerful and cheap photocatalyst is an important constituent.[5] Recently, Kalantar-zadeh *et al.* [6] demonstrated that the intriguing properties of two-dimensional transition metal dichalcogenides have led to a significant body of fundamental research and rapid uptake of these materials in photocatalytic application. Zhang *et al.* reported that $Ga_2O_3$ nanoparticles are incorporated into liquid metal/metal oxide frameworks in order to form enhanced photocatalytic systems using solvothermal method.[7,8] CV dye degradations were studied using several systems that generated active species, including BiOI,[9] $Bi_xAg_yO_z$,[10] $Bi_2WO_6$,[11] $TiO_2$,[12] ZnO,[13] and $BaTiO_3$.[14]

Recently, the development of visible-light-sensitive photocatalysts has obtained considerable attention as an alternative for wastewater treatment. An effective and simple strategy to improve the photocatalytic activity of a photocatalyst is the incorporation of a heterostructure,

[a] Department of Science Education and Application, National Taichung University of Education, Taichung 403, Taiwan
[b] Department of Occupational Safety and Health, Chung-Shan Medical University, Taichung 402, Taiwan
[c] Department of Occupational Medicine, Chung-Shan Medical University Hospital, Taichung 402, Taiwan
* Author to whom correspondence should be addressed
E-mail: ccchen@mail.ntcu.edu.tw ; wllee01@csmu.edu.tw
Fax: +886-4-2218-3560
Tel: +886-4-2218-3406/+886-4-24730022

because heterojunctions have great potential for tuning the desired electronic properties of photocatalysts and efficiently separating the photogenerated electron–hole pairs.[15-17]

In recent years, as a new family of advantageous photocatalysts, the bismuth oxyhalides have showed unusual photocatalytic activities because their unique layered structure features an internal static electric field vertical to each layer that may cause more effective separation of photogenerated charge carriers.[18-20] Among the bismuth oxyhalides,[21,22] bismuth oxyiodides have obtained remarkable interests in recent years because of their suitable band gaps, stability, and relatively superior photocatalytic activities. It is found that the BiOI composite (i.e. $Bi_4O_5Br_2$/BiOI) shows higher photocatalytic activities than BiOBr compositesand BiOCl composites for the photocatalytic degradation of methyl orange or crystal violet do.[23-26]

Since the valence band for bismuth oxyiodides mostly contained $O_{2p}$ and $I_{5p}$ orbitals, while the conduction band was based on the $Bi_{6p}$ orbital,[27] it could be demonstrated that the I-poor bismuth oxyiodides had the band-gap energy higher than BiOI but lower than $Bi_2O_3$;[28,29] hence, these materials might be used as visible-light responsivephotocatalysts. More importantly, the structure and composition of the bismuth oxyiodides strongly influenced their electronic, optical, and oxidizing abilities and other physicochemical properties, proposing an opportunity to acquire novel photocatalysts for effective degradation of environmental and toxic pollutants. However, the synthesis methods, characterization, and evaluated properties of a series bismuth oxyiodides remained rare until recently.

In the search for robust and stable visible-light-driven semiconductorphotocatalysts, a polymeric semiconductor, graphitic carbon nitride (g-$C_3N_4$), has recently attracted tremendous attention. The heptazine ring structure and high condensation degree enable metal-free g-$C_3N_4$ to possess many advantages such as good physicochemical stability, as well as an appealing electronic structure combined with a medium-band gap (2.7 eV).[30] These unique properties make g-$C_3N_4$ a promising candidate for visible light photocatalytic applications utilizing solar energy.

It is believed that there is a close relationship between the size, morphology and the properties of photocatalysts. Therefore, photocatalysts with hierarchical architectures are expected to exhibit enhanced photocatalytic performance. It is expected that functionalizing graphitic carbon nitride nanosheets with bismuth oxyhalide can not only combine both the advantages of bismuth oxyhalide and graphitic carbon nitride nanosheets but may also result in new properties. Recently, BiOCl/g-$C_3N_4$, [31] BiOBr/g-$C_3N_4$, [32] BiOI/g-$C_3N_4$, [33,34] and $BiOBr_{0.2}I_{0.8}$ [35] composites have been synthesized in order to improve the photocatalytic activity of the materials. However, no work compared to g-$C_3N_4$ based on a series of bismuth oxyiodide photocatalysts has been reported.

To the best of our knowledge, $BiO_xI_y$/g-$C_3N_4$-assisted photocatalytic degradation of TPM dye under visible light irradiation has never been reported in the literature. This is the first report thatfour $BiO_xI_y$/g-$C_3N_4$ composites namely, BiOI/g-$C_3N_4$, $Bi_7O_9I_3$/g-$C_3N_4$, $Bi_5O_7I$/g-$C_3N_4$, and $Bi_7O_9I_3$/$Bi_5O_7I$/g-$C_3N_4$ have been isolated and characterized by by FE-SEM-EDS, XRD, HR-XPS, and UV-vis-DRS. Through degrading CV in aqueous solutions under visible-light irradiation, the photocatalytic activities of these four $BiO_xI_y$/g-$C_3N_4$ composites are further compared and discussed.

# 2. Experiment

## 2.1 Materials

$Bi(NO_3)_3$•$5H_2O$, KI (Katayama), CV dye (TCI), *p*-benzoquinone (Alfa aesar), sodium azide (Sigma), ammonium oxalate (Osaka), and isopropanol (Merck) were purchased and used without further purification. Reagent-grade sodium hydroxide, nitric acid, ammonium acetate, and HPLC-grade methanol were obtained from Merck.

## 2.2 Instruments and analytical methods

The field-emission transmission electron microscopy (FE-TEM) images, selected area electron diffraction (SAED) patterns, high resolution transmission electron microscopy (HRTEM) images, and energy-dispersive X-ray spectra (EDS) were obtained using a JEOL-2010 with an accelerating voltage of 200 kV. The Al-Kα radiation was generated at 15 kV. The X-ray diffraction (XRD) patterns were recorded on a MAC Science MXP18 equipped with Cu-Kα radiation, operating at 40 kV and 80 mA. Field emission scanning electron microscopy-electron dispersive X-ray spectroscopy (FE-SEM-EDS) measurements were carried out using a JEOL JSM-7401F at an acceleration voltage of 15 kV. High resolution X-ray photoelectron spectroscopy (HRXPS) measurements were carried out using an ULVAC-PHI. Photoluminescence (PL) measurements were carried out on Hitachi F-7000. The Ultra-violet photoelectron spectroscopy (UPS) measurements were performed using a ULVAC-PHI XPS, PHI Quantera SXM. The Brunauer-Emmett-Teller (BET) specific surface areas of the samples ($S_{BET}$) were measured with an automated system (Micrometrics Gemini) using nitrogen gas as the adsorbate at liquid nitrogen temperature. The HPLC-PDA-ESI-MS system consisted of a Waters 1525 binary pump, 2998 photodiode array detector, and 717 plus autosampler, a ZQ2000 micromass detector.



 

### 2.3 Synthesis of different $BiO_xI_y$/g-$C_3N_4$ composites

Under atmosphere conditions, the g-$C_3N_4$ powder was synthesized by directing calcining melamine in a muffle furnace. In a typical synthesis run, 5 g melamine was placed in a semi-closed alumina crucible with a cover. The crucible was heated to 520 °C for 4 h with a heating rate 10 °C/min. After cooling to room temperature, g-$C_3N_4$ was produced in a powder form. [36] 5 mmol Bi $(NO_3)_3$•$5H_2O$ was first mixed in a 50 mL flask, and followed by adding 5 mL 4M ethylene glycercol and g-$C_3N_4$ powder. With continuous stirring, 2 M NaOH was added dropwiseto adjust the pH value; and, when a precipitate was formed, 2 mL KI was also added dropwise. The solution was then stirred vigorously for 30 min and transferred into a 30 mL Teflon-lined autoclave, which was heated up to 150 °C in 30 minute and maintained for 12h and then naturally cooled down to room temperature.[6] The resulting solid precipitate was collected by filtration, washed with deionized water and methanol to remove any possible ionic species in the solid precipitate, and then dried at 60°C overnight. Depending on the pH value, different $BiO_xI_y$/g-$C_3N_4$ composites could be synthesized.

### 2.4 Photocatalytic experiments

The CV irradiation experiments were carried out on stirred aqueous solution contained in a 100-mL flask; the aqueous suspension of CV (100 mL, 10 ppm) and the amount of catalyst powder were placed in a Pyrex flask. The pH of the suspension was adjusted by adding either NaOH or $HNO_3$ solution. Dark experiments were performed in order to examine the adsorption/desorption equilibrium. 10 mg of the photocatalyst was mixed with 100mL CV aqueous solution with a known initial concentration, in a 100mL flask and the mixture shaken in an orbital shaker (100 rpm) at a constant temperature. The mixture was centrifuged at 3000 rpm in a centrifugation machine after batch sorption experiments so that the absorbance of CV could be determined at 580nm by means of HPLC-PDA. The concentrations of the solutions were determined using linear regression equation. Prior to irradiation, the suspension was magnetically stirred in dark for ca. 30 min to establish an adsorption/desorption equilibrium between the CV and the catalyst surface. Irradiation was carried out using 150 W Xe arc lamps; the light intensity was fixed at 31.2 W/$m^2$, and the reaction vessel was placed 30 cm from the light source. At given irradiation time intervals, a 5-mL aliquot was collected and centrifuged to remove the catalyst. The supernatant was measured by HPLC-PDA.

A series of quenchers were introduced to scavenge the relevant active species in order to evaluate the effect of the active species during the photocatalytic reaction. $O_2^{\bullet-}$, $^{\bullet}OH$, $h^+$, and $^1O_2$ were studied by adding 1.0 mM benzoquinone (BQ, a quencher of $O_2^{\bullet-}$), [37] 1.0 mM isopropanol (IPA, a quencher of $^{\bullet}OH$), [38] 1.0 mM ammonium oxalate (AO, a quencher of $h^+$), [39] and 1.0 mM sodium azide (SA, a quencher of $^1O_2$, [40] respectively. The method was similar to the former photocatalytic activity test.

## 3. Results and discussion

### 3.1 Characterization of $BiO_xI_y$/g-$C_3N_4$ Composites

#### 3.1.1 Phase, morphology, and composition

**Figure 1** shows the XRD patterns of the as-prepared samples; the patterns clearly show the existence of different $BiO_xI_y$ phases composite with g-$C_3N_4$. All the samples as-prepared contain the BiOI phase (JCPDS73-2062), $Bi_7O_9I_3$ phase, [41] $Bi_5O_7I$ phase (JCPDS 40-0548), and g-$C_3N_4$ (JCPDS 87-1526), in addition to the $Bi_6O_5(OH)_3(NO_3)_3$•$2H_2O$ (JCPDS 54-0624) phases. At pH = 1, the XRD patterns (**Figure 1(a)**) are identical to those reported for the BiOI/g-$C_3N_4$ binary phases; at pH = 4, the XRD patterns (**Figure 1(b)**) are identical to those reported for the BiOI/g-$C_3N_4$ binary phases at 5-90wt% and BiOI/$Bi_6O_5(OH)_3(NO_3)_3$•$2H_2O$/g-$C_3N_4$ ternary phases at 95wt%; at pH= 7, the XRD patterns (**Figure 1(c)**) are identical to those reported for the $Bi_7O_9I_3$/g-$C_3N_4$ binary phases; at pH= 10, the XRD patterns (**Figure 1(d)**) are identical to those reported for the $Bi_7O_9I_3$/$Bi_5O_7I$/g-$C_3N_4$ ternary phases; and at pH= 13, the XRD patterns (**Figure 1(d)**) are identical to those reported for the $Bi_5O_7I$/g-$C_3N_4$ binary phases. **Table 1** summarizes the results of the XRD measurements.

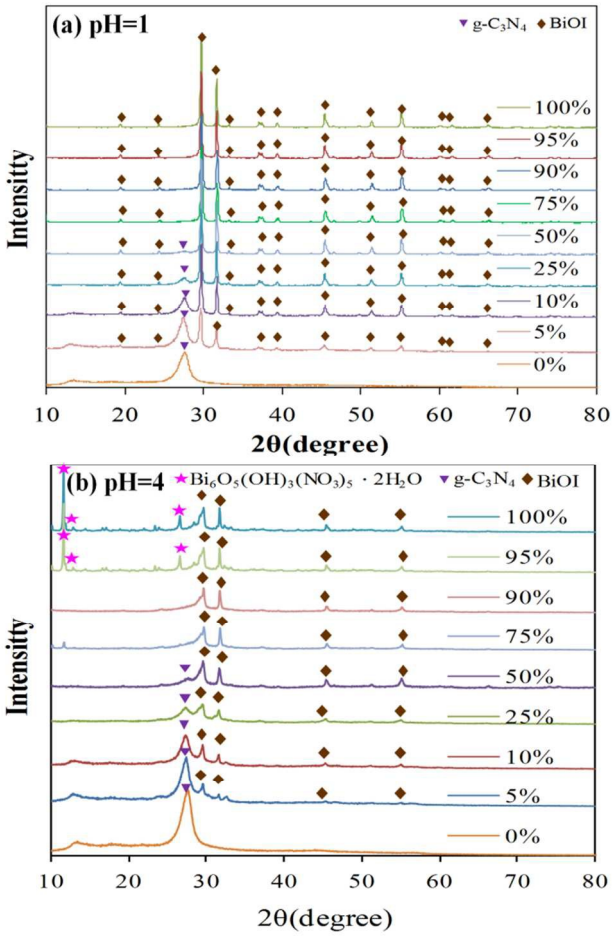

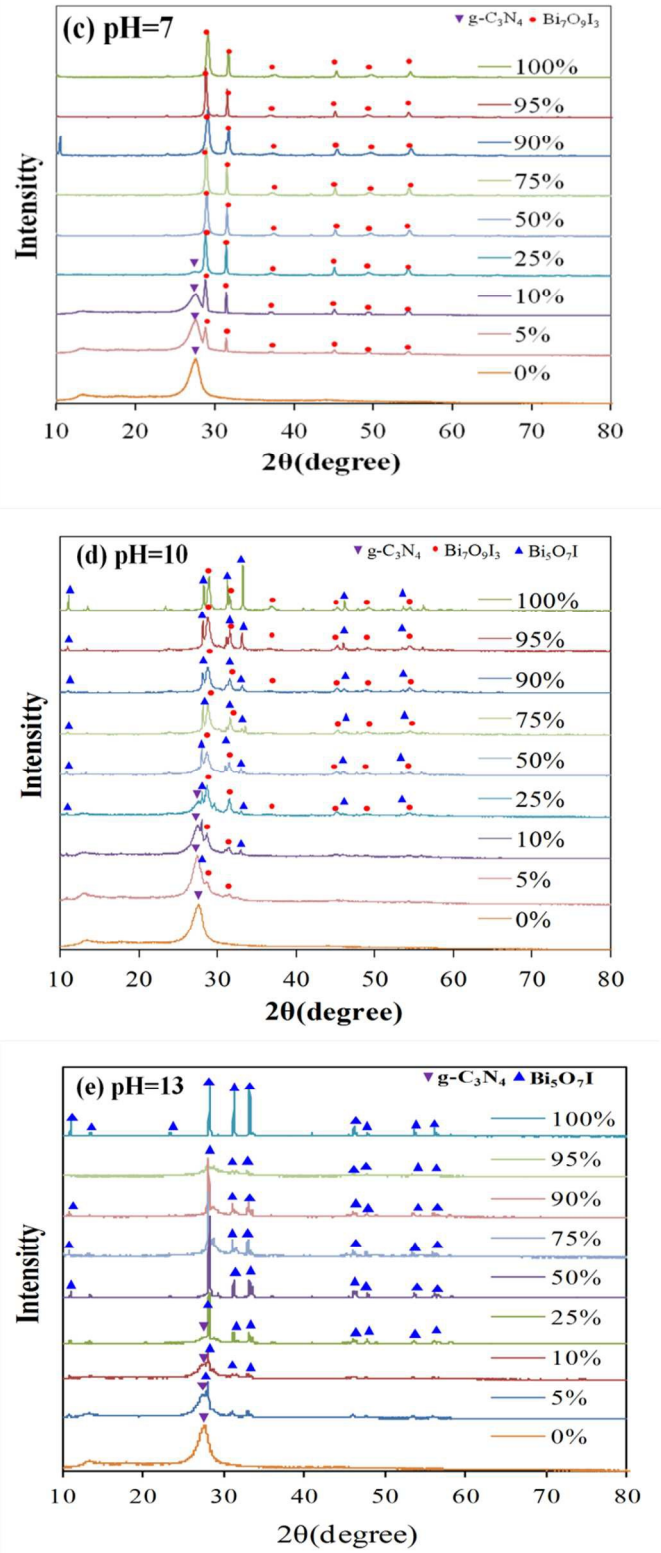


**Figure 1.** XRD patterns of as-prepared $BiO_xI_y$/g-$C_3N_4$ samples under different pH values

**Table 1.**Crystalline phase changes of $BiO_xI_y$/g-$C_3N_4$ prepared under different reaction conditions. (◆BiOI; ●$Bi_7O_9I_3$; ▲$Bi_5O_7I$; ▼g-$C_3N_4$; ★$Bi_6O_5(OH)_3(NO_3)_5$•$2H_2O$)

| $BiO_xI_y$/g-$C_3N_4$ | | | | | |
|---|---|---|---|---|---|
| Bismuth oxyiodide Weight(%) | pH | | | | |
| | 1 | 4 | 7 | 10 | 13 |
| 0 | ▼ | ▼ | ▼ | ▼ | ▼ |
| 5 | ▼◆ | ▼◆ | ▼● | ▼●▲ | ▼▲ |
| 10 | ▼◆ | ▼◆ | ▼● | ▼●▲ | ▼▲ |
| 25 | ▼◆ | ▼◆ | ▼● | ▼●▲ | ▼▲ |
| 50 | ▼◆ | ▼◆ | ▼● | ▼●▲ | ▼▲ |
| 75 | ▼◆ | ▼◆ | ▼● | ▼●▲ | ▼▲ |
| 90 | ▼◆ | ▼◆★ | ▼● | ▼●▲ | ▼▲ |
| 95 | ▼◆ | ▼◆★ | ▼● | ▼●▲ | ▼▲ |
| 100 | ◆ | ◆★ | ● | ●▲ | ▲ |

**Figures 2-6** displays that the as-prepared samples are composed of differently sized layers, consistent with the TEM observations. In addition, the EDS spectrum shows that the sample contains the elements of Bi, I, O, C, and N. In **Figure 2**, the HRTEM image shows that two sets of different lattice images are found with a d-spacing of 0.282 nm, corresponding to the (110) plane of BiOI, which is in good agreement with the XRD results (**Figure 1(a)**). In **Figure 3**, the HRTEM image shows that two sets of different lattice images are found with a d-spacing of 0.240 nm, corresponding to the (112) plane of BiOI, which is in good agreement with the XRD results (**Figure 1(b)**). In **Figure 4**, the HRTEM image shows that two sets of different lattice images are found with a d-spacing of 0.314 nm, corresponding to the (110) plane of $Bi_7O_9I_3$, which is in good agreement with the XRD results (**Figure 1(c)**). In **Figure 5**, the HRTEM image shows that three sets of different lattice images are found with a d-spacing of 0.286 and 0.306 nm, corresponding to the (110) plane of $Bi_7O_9I_3$ and $Bi_5O_7I$, which is in good agreement with the XRD results (**Figure 1(d)**). In **Figure 6**, the HRTEM image shows that two sets of different lattice images are found with a d-spacing of 0.319 nm, corresponding to the (312) plane of BiOI, which is in good agreement with the XRD results (**Figure 1(e)**). The results suggest that the $BiO_xI_y$/g-$C_3N_4$ phases have been produced in the composites, which are favorable for the separation of photo-induced carriers, yielding high photocatalytic activities.

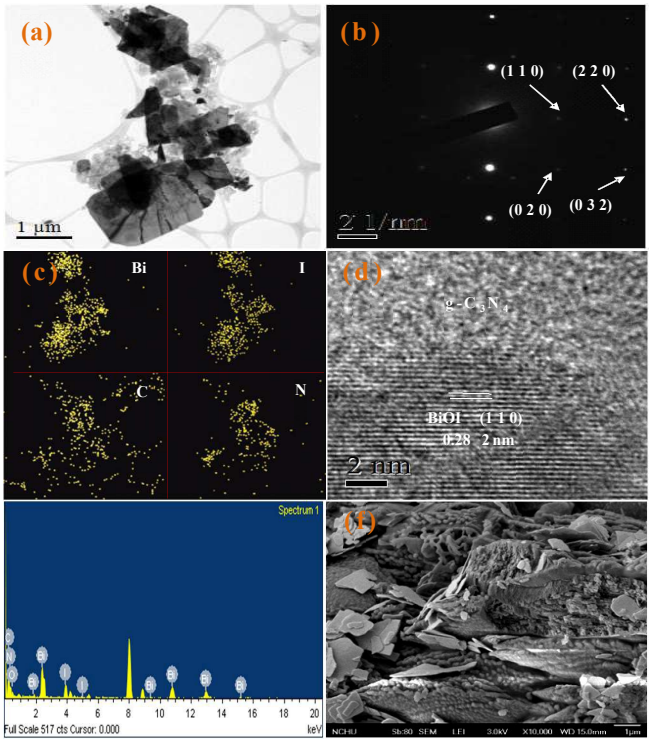


**Figure 2.** FE-TEM and FE-SEM of as-prepared BiOI/g-$C_3N_4$ (pH=1, 50wt%).

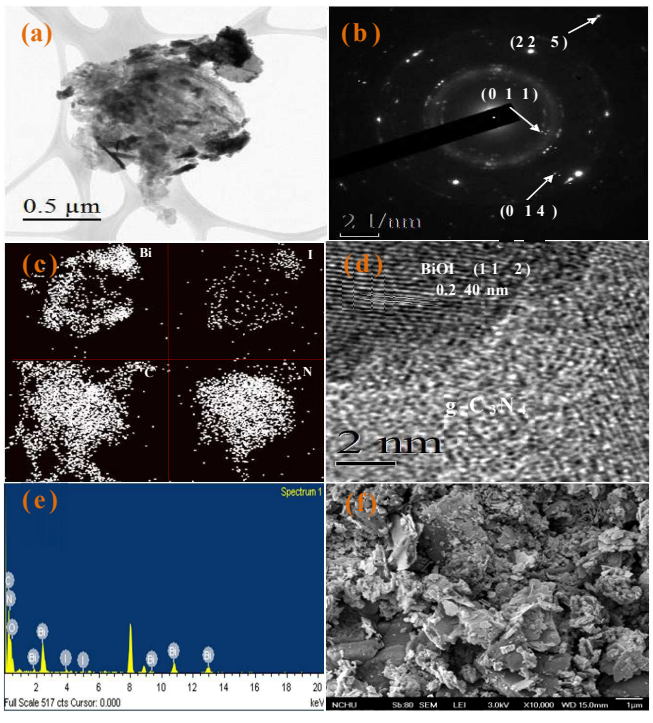


**Figure 3.** FE-TEM and FE-SEM of as-prepared BiOI/g-$C_3N_4$ (pH=4, 50wt%).

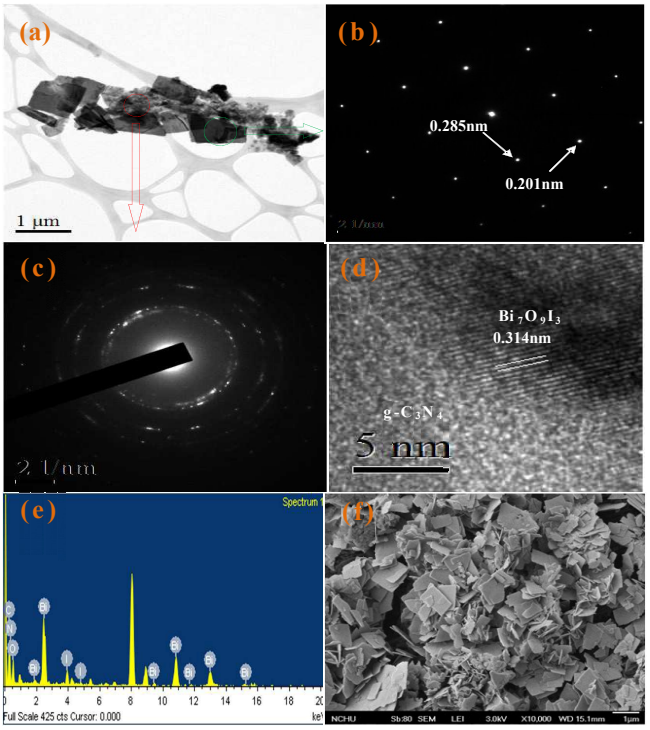


**Figure 4.** FE-TEMand FE-SEM of as-prepared $Bi_7O_9I_3$/g-$C_3N_4$ (pH=7, 50wt%).

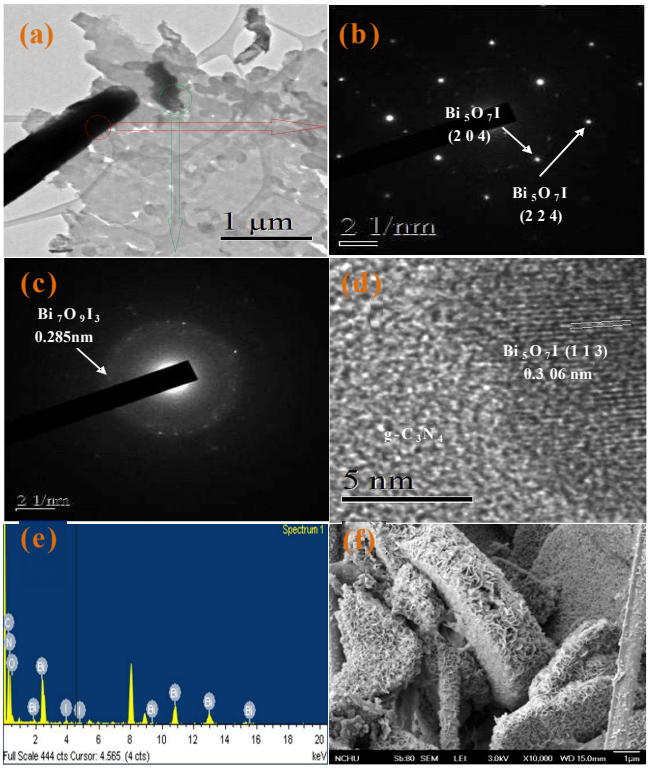


**Figure 5.** FE-TEM and FE-SEM of as-prepared $Bi_5O_7I$/g-$C_3N_4$ (pH=10, 50wt%).

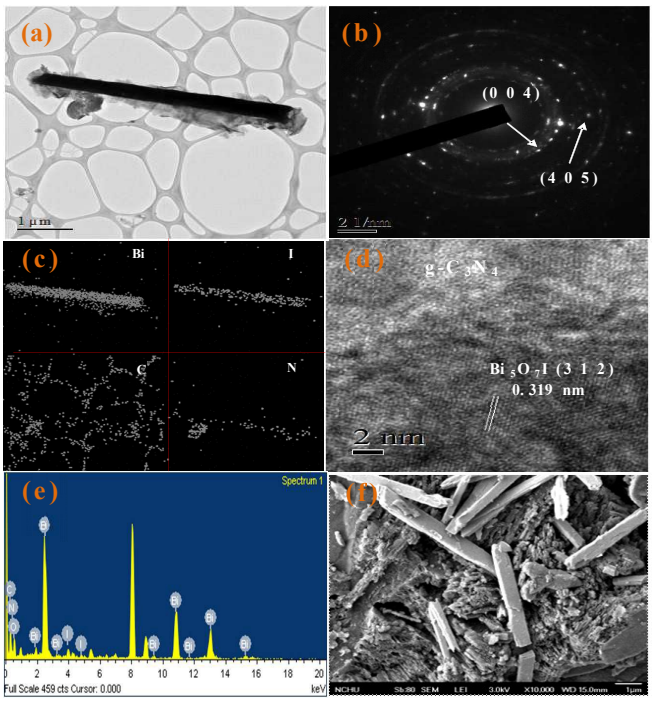


**Figure 6.** FE-TEMand FE-SEM of as-prepared $Bi_5O_7I$/g-$C_3N_4$ (pH=13, 50wt%).

Our group[6] revealed that the controllable morphologies and crystal phases of bismuth oxyiodides could be completed by simply changing some growth parameters, including pH values, molar ratio, and hydrothermal temperature. BiOI was obtained at low pH values; $Bi_7O_9I_3$ was obtained at middle pH values; $Bi_5O_7I$ was obtained at high pH values. This reference demonstrated that BiOI was formed at the beginning of the hydrothermal reaction, and then $OH^-$ gradually substituted $I^-$ in the basic conditions, which resulted in the reduced content of $I^-$ in the samples. Increasing the pH to gradually acquire BiOI, $Bi_4O_5I_2$, $Bi_7O_9I_3$, $Bi_5O_7I$, and α-$Bi_2O_3$, the higher the pH value appeared the lower the $I^-$content in the samples, until the content of $I^-$ in the products was fully replaced by $OH^-$ and finally resulted in the formation of α-$Bi_2O_3$ under strong basic conditions. The detailed statements about the effect of reaction temperature and molar ratio are described in the reference.

The results illustrate that, a series of changes happen in the product distribution at different pH value. The proposed processes for the formation of $BiO_xI_y$/g-$C_3N_4$ composites are described in equations 1–7. The results demonstrate a series of changes in the compounds prepared at different hydrothermal conditions, expressed as BiOI → $Bi_4O_5I_2$ → $Bi_7O_9I_3$ → $Bi_5O_7I$ → α-$Bi_2O_3$. By controlling the pH of the hydrothermal reaction, different compositions of bismuth oxyiodides are acquired as follows.

$$Bi^{3+} + 3OH^- \rightarrow Bi(OH)_{3(s)} \quad (1)$$

$$2Bi(OH)_3 + I^- + g\text{-}C_3N_4 \rightarrow BiOI/g\text{-}C_3N_4 + H_2O + OH^- \quad (2)$$

$$4BiOI + 2OH^- + g\text{-}C_3N_4 \rightarrow Bi_4O_5I_2/g\text{-}C_3N_4 + 2I^- + H_2O \quad (3)$$

$$7Bi_4O_5I_2 + 2OH^- + g\text{-}C_3N_4 \rightarrow 4Bi_7O_9I_3/g\text{-}C_3N_4 + 2I^- + H_2O \quad (4)$$

$$3Bi_7O_9I_3 + 2OH^- + g\text{-}C_3N_4 \rightarrow 7Bi_3O_4I/g\text{-}C_3N_4 + 2I^- + H_2O \quad (5)$$

$$5Bi_3O_4I + 2OH^- + g\text{-}C_3N_4 \rightarrow 3Bi_5O_7I/g\text{-}C_3N_4 + 2I^- + H_2O \quad (6)$$

$$2Bi_5O_7I + 2OH^- + g\text{-}C_3N_4 \rightarrow 5Bi_2O_3/g\text{-}C_3N_4 + 2I^- + H_2O \quad (7)$$

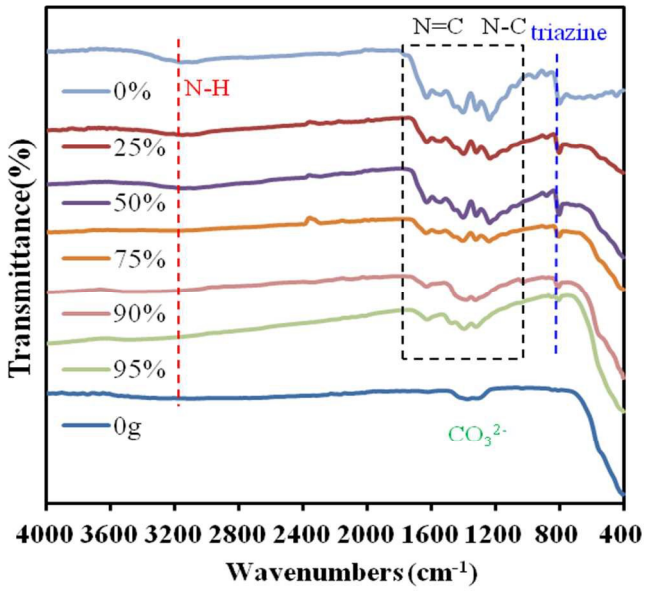


**Figure 7.** FT-IR of as-prepared $Bi_7O_9I_3$/$Bi_5O_7I$/g-$C_3N_4$ samples under pH 10.

A series of $BiO_xI_y$/g-$C_3N_4$ compositesare synthesized by hydrothermal methods at different pH values. The surface morphologies of the as-prepared samples (**Figures 2-6(f)**) are measured by FE-SEM-EDS. The FE-SEM image displays that the morphologies of the samples acquired at different pH values turn from irregular nano-thin-sheets to irregular particles and square thin-plates then become irregular rods. The SEM-EDS and TEM-EDS results demonstrate that the main elements within these samples are carbon, nitrogen, oxygen, iodine, and bismuth at **Figure 2-6(e)**. The Bi/I atomic ratios of the bismuth oxyiodide samples were within the range of 1.08-165.43, which corresponded to BiOI, $Bi_4O_5I_2$, $Bi_7O_9I_3$, $Bi_5O_7I$, and α-$Bi_2O_3$ phase, compared to the stoichiometric ratio (Bi: I = 1, 2, 2.3, 5, ∞), and could be selectively

synthesized through a hydrothermal method. The possible processes for the synthesis of bismuth oxyiodides were described as eqs. 1-8. From above results, a series of $BiO_xI_y$/g-$C_3N_4$ composites could be selectively synthesized through a controlled hydrothermal method.

**Figure 7** shows the FT-IR spectra of the $Bi_7O_9I_3$/$Bi_5O_7I$/g-$C_3N_4$ composite produced under different weight percentage, where the strong absorption mainly locate in the 400–700 $cm^{-1}$, as a result of the stretching vibrations of Bi−O, Bi−O−I, and Bi−O−Bi in bismuth oxyiodides.[42] With therelation to pure g-$C_3N_4$, the peaks at 1252, 1326, 1420, 1572, and 1640 $cm^{-1}$ correspond to the typical stretching modes of the CN heterocycles.[43] Additionally, the characteristic breathing mode of the triazine units at 811 $cm^{-1}$ is observed.[44] This result agrees with that of the XRD and TEM experiment.

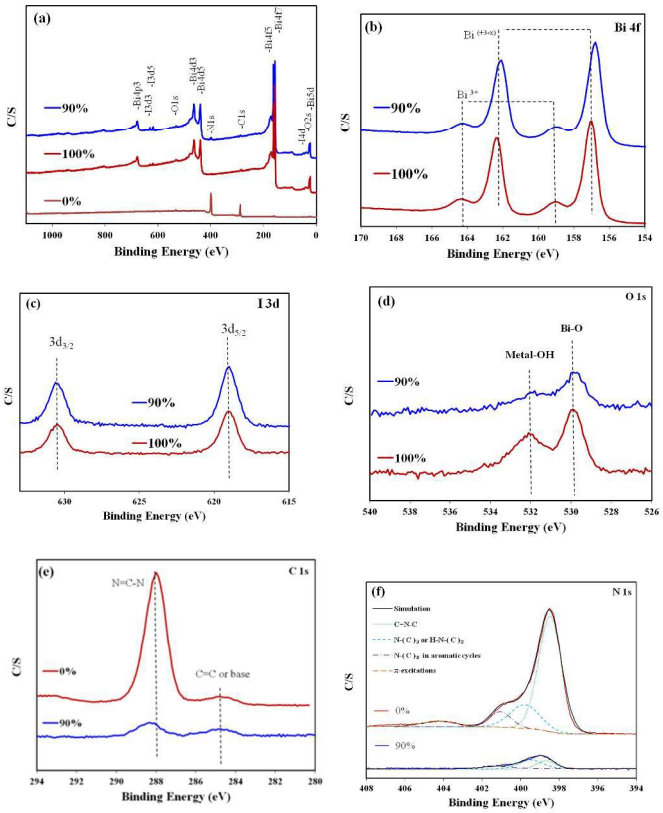


**Figure 8.** XPS of $Bi_7O_9I_3$/$Bi_5O_7I$/g-$C_3N_4$( pH =10) (a) Total survey, (b) Bi-4f, (c) I-3d, (d) O-1s, (e) C-1s, (f) N-1s.

### 3.1.2 X-ray photoelectron spectroscopy analysis

**Figure 8** presents the Bi 4f, I 3d, O 1s, C 1s, and N 1s XPS spectra of the $Bi_7O_9I_3$/g-$C_3N_4$ composites. Observation of the transition peaks involving the Bi 4f, I 3d, O 1s, C 1s, and N 1s orbitals identifies that the catalysts are composed of Bi, I, O, C, and N. The characteristic binding energy value of 159.1 eV for Bi $4f_{7/2}$**(Figure 8(b))** shows a trivalent oxidation state for bismuth. An additional spin–orbit doublet with the binding energy of 156.5 eV for Bi $4f_{7/2}$ is also revealed in all samples, suggesting that certain parts of bismuth exist in the (+3-x) valence state. This shows that the trivalent bismuth partially reduces to the lower valence state by the hydrothermal method. A similar chemical shift of approximately 2.1 eV for Bi $4f_{7/2}$ was also published by Liao *et al*.[42,45] They summarized that Bi $^{(+3-x)}$ formal oxidation state could most probably be ascribed to the sub-stoichiometric forms of Bi within the $Bi_2O_2$ layer, and the formation of the low oxidation state resulted in oxygen vacancy in the crystal lattice. However, it is supposed in this study that Bi $^{(+3-x)}$ formal oxidation state could most likely be ascribed to the sub-stoichiometric forms of Bi at the outer site of the particles, and the formation of the low oxidation state results in oxygen vacancy in the crystal surface, revealing that the main chemical states of the bismuth element in the samples are not trivalent. A shift of the Bi $^{(+3-x)}$ peak of 100% sample compared to that of 90% sample, the shift in binding energy of approximately 0.5 eV for Bi $4f_{7/2}$ photoelectrons does exhibit minor change with adding 10wt% g-$C_3N_4$, as a result of Bi−N bond in $Bi_7O_9I_3$/$Bi_5O_7I$/g-$C_3N_4$.

From **Figure 8(c)**, the binding energy of 630.6 eV and 619.0 eV are attributed to I $3d_{5/2}$ and $3d_{3/2}$ respectively, which could be pointed to I at the monovalent oxidation state. The asymmetric O 1s peak shown in **Figure 8(d)** can be split by using the XPS peak-fitting program. The peak at 531.3 eV is assigned to the external −OH group or the water molecule adsorbed on the surface, and the other O 1s peak appearing at 529.9 eV corresponds to lattice oxygen atoms in the $BiO_xCl_y$/$BiO_mI_n$.[16] **Figure 8(e)** shows the high resolution C 1s spectrum of $Bi_7O_9I_3$/g-$C_3N_4$ composites. There are mainly two carbon species displayed in the C 1s spectra.One (284.7 eV) is $sp^2$ C−C bonds, and the other (287.9 eV) is $sp^2$-hybridized carbon in N-containing aromatic ring (N−C＝N). The latter is indicated as the major carbon species in polymeric g-$C_3N_4$.[46] In **Figure 8(f)**, three peaks are deconvoluted for N1s spectra. The highest peak centering at 398.5 eV is assigned as the $sp^2$-hybridized nitrogen involved in triazine rings (C−N = C), whereas the peak at 401.1 eV corresponds to the tertiary nitrogen N−$(C)_3$ groups. Both of them, together with $sp^2$-hybridized carbon (N−C = N, 287.9 eV), compose the heptazine heterocyclic ring units, constructing the basic substructure units of g-$C_3N_4$ polymers. The weak peak at 404.3 eV is characterized to charging effects or positive charge localization in heterocycles.[44]

### 3.1.3 Optical absorption properties

As shown in **Figures 9** and **Figure S1-S4** of ESI† for DR-UV of the various $BiO_xI_y$/g-$C_3N_4$ composites, the absorption edge of the pure g-$C_3N_4$ is at about 482.5 nm, which originates from its band gap of 2.57 eV and is consistent with the reported results.[47] Pure g-$C_3N_4$ absorbs only a small amount of visible light, whereas the absorption edge of $BiO_xI_y$ extends across the entire visible light spectrum.The $E_g$ value of $BiO_xI_y$/g-$C_3N_4$ is determined from a plot of $(\alpha hv)^{1/2}$ vs energy ($hv$), which is calculated as 1.32–2.51 eV (**Table S1**of ESI†). The results suggest that the fabrication of the heterostructured $BiO_xI_y$/g-$C_3N_4$ can greatly improve the optical absorption property and increase the utilized efficiency of solar light, which are favorable for the enhancement of the photocatalytic activity.

### 3.1.4 Adsorption-desorption isotherm

**Figures 10** and **Figure S5-S8** of ESI† show the nitrogen adsorption-desorption isotherm curves of $BiO_xI_y$, g-$C_3N_4$ and $BiO_xI_y$/g-$C_3N_4$. The isotherms of all the samples are close to Type IV with a hysteresis loop at a high relative pressure between 0.6 and 1.0.[42,48] The shape of the hysteresis loop is close to Type H3, suggesting the existence of slit-like pores generally formed by the aggregation of plate-like particles, which is consistent with the self-assembled nanoplate-like morphology of samples. This result is consistent with the FE-SEM results, showing that self-assembled nanosheets or nanoplates result in the formation of hierarchical architectures.

### 3.2 Photocatalytic Activity

The degradation efficiency as a function of reaction time is illustrated in **Figure 11**; the removal efficiency is significantly enhanced in the presence of 90-95wt% $Bi_7O_9I_3$/$Bi_5O_7I$/g-$C_3N_4$. After irradiation for 48 h, 95wt% $Bi_7O_9I_3$/$Bi_5O_7I$/g-$C_3N_4$ exhibits a superior photocatalytic performance, with the CV removal efficiency up to 99%. To further understand the reaction kinetics of CV degradation, the apparent pseudo-first-order modelexpressed by $\ln(C_o/C) = kt$ equation is applied in the experiments.[49] Via the first-order linear fit of the data shown in **Figure 11(b)** and **Table 2**, the k value of 95wt% $Bi_7O_9I_3$/$Bi_5O_7I$/g-$C_3N_4$ is obtained as the maximum degradation rate of $1.70 \times 10^{-1}$ $h^{-1}$ using the first-order linear fit of the data, which is much higher than that of the other composites; the 95wt% $Bi_7O_9I_3$/$Bi_5O_7I$/g-$C_3N_4$ composite is a much more effective photocatalyst than the others synthesized in this study. The 95wt% $Bi_7O_9I_3$/$Bi_5O_7I$/g-$C_3N_4$ composite has larger $S_{BET}$ and pore volume (**Table S2** of ESI†). However, the result of **Table S2** of ESI† shows that the 95wt% $Bi_5O_7I$/g-$C_3N_4$ sample—which shows the highest $S_{BET}$—does not represent the highest photocatalytic activity ($k = 1.17\times 10^{-1}$ $h^{-1}$) among the samples, suggesting that the changes in the photocatalytic activity is resulted from both $S_{BET}$ and $BiO_xI_y$/g-$C_3N_4$ composites. Comparison of rate constant by different photocatalysts is shown in **Table 3**. The order of rate constant is as $Bi_7O_9I_3$/$Bi_5O_7I$/g-$C_3N_4$ > $Bi_5O_7I$/g-$C_3N_4$ > $Bi_7O_9I_3$/$Bi_5O_7I$ > $Bi_7O_9I_3$/g-$C_3N_4$ > BiOI/g-$C_3N_4$ > $Bi_7O_9I_3$ > $Bi_5O_7I$ > g-$C_3N_4$ > BiOI. The photocatalytic activity of the $Bi_7O_9I_3$/$Bi_5O_7I$/g-$C_3N_4$ heterojunctons reaches the maximum rate constant of 0.170 $h^{-1}$, 5 times higher than that of BiOI, 4 times higher than that of g-$C_3N_4$, and 1.5 times higher than that of $Bi_7O_9I_3$/$Bi_5O_7I$. Thus, the $BiO_xI_y$/g-$C_3N_4$ and $Bi_7O_9I_3$/$Bi_5O_7I$ composites may also play a role in enhancing the photocatalytic activity.

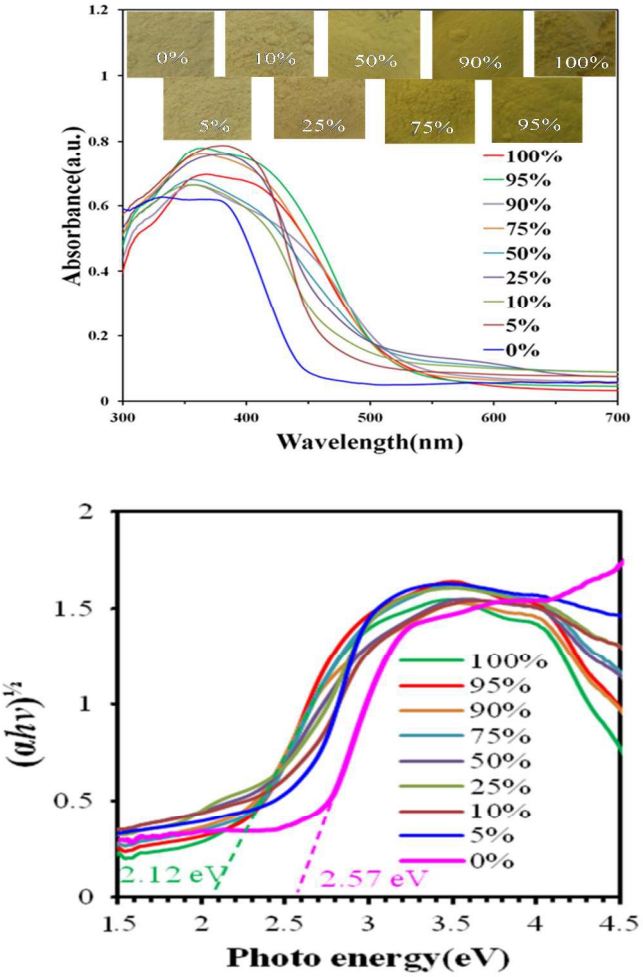


**Figure 9.** DRS patterns of as-prepared $Bi_7O_9I_3$/$Bi_5O_7I$/g-$C_3N_4$ samples under pH 10.

**Table 2.** The pseudo-first-order rate constants for thedegradation ofCV with $BiO_xI_y$/g-$C_3N_4$photocatalysts.

| Bismuth oxyiodide/g-$C_3N_4$ | | | | | | | | | | |
|---|---|---|---|---|---|---|---|---|---|---|
| Bismuth oxyiodide Weight(%) | pH | | | | | | | | | |
| | 1 | | 4 | | 7 | | 10 | | 13 | |
| | k($h^{-1}$) | $R^2$ | k($h^{-1}$) | $R^2$ | k($h^{-1}$) | $R^2$ | k($h^{-1}$) | $R^2$ | k($h^{-1}$) | $R^2$ |
| 0 | 0.042 | 0.971 | 0.036 | 0.997 | 0.033 | 0.999 | 0.033 | 0.999 | 0.035 | 0.998 |
| 5 | 0.024 | 0.906 | 0.025 | 0.912 | 0.039 | 0.992 | 0.036 | 0.903 | 0.018 | 0.907 |
| 10 | 0.022 | 0.952 | 0.028 | 0.921 | 0.041 | 0.983 | 0.042 | 0.902 | 0.042 | 0.918 |
| 25 | 0.039 | 0.971 | 0.023 | 0.908 | 0.042 | 0.987 | 0.054 | 0.903 | 0.057 | 0.913 |
| 50 | 0.012 | 0.948 | 0.036 | 0.949 | 0.071 | 0.987 | 0.112 | 0.910 | 0.021 | 0.901 |
| 75 | 0.018 | 0.947 | 0.021 | 0.901 | 0.047 | 0.992 | 0.118 | 0.979 | 0.099 | 0.979 |
| 90 | 0.035 | 0.977 | 0.032 | 0.947 | 0.103 | 0.975 | 0.169 | 0.989 | 0.110 | 0.992 |
| 95 | 0.019 | 0.943 | 0.028 | 0.939 | 0.102 | 0.981 | 0.170 | 0.988 | 0.117 | 0.994 |
| 100 | 0.033 | 0.931 | 0.043 | 0.906 | 0.053 | 0.986 | 0.123 | 0.983 | 0.044 | 0.969 |

As shown in **Table 4**, $BiO_xI_y$/g-$C_3N_4$ has obtained remarkable interests in recent years because of their suitable band gaps, stability, and relatively superior photocatalytic activities. It is found that the $BiO_xI_y$/g-$C_3N_4$ composite shows higher photocatalytic activities than $BiO_xI_y$ and g-$C_3N_4$ for the photocatalytic degradation of rhodamine B (or methyl blue, methyl organge, crystal violet, bisphenol A, 4-chlorophenol) do.[50-54]

**Table 3.**Comparison of rate constant by different photocatalyst.

| Photocatalyst | Rate Constant, k ($h^{-1}$) |
|---|---|
| g-$C_3N_4$ | 0.042 |
| BiOI | 0.033 |
| $Bi_7O_9I_3$ | 0.053 |
| $Bi_5O_7I$/ $Bi_7O_9I_3$ | 0.123 |
| $Bi_5O_7I$ | 0.044 |
| BiOI / g-$C_3N_4$ | 0.035 |
| $Bi_7O_9I_3$ / g-$C_3N_4$ | 0.103 |
| $Bi_5O_7I$/ $Bi_7O_9I_3$ / g-$C_3N_4$ | 0.170 |
| $Bi_5O_7I$/ g-$C_3N_4$ | 0.117 |

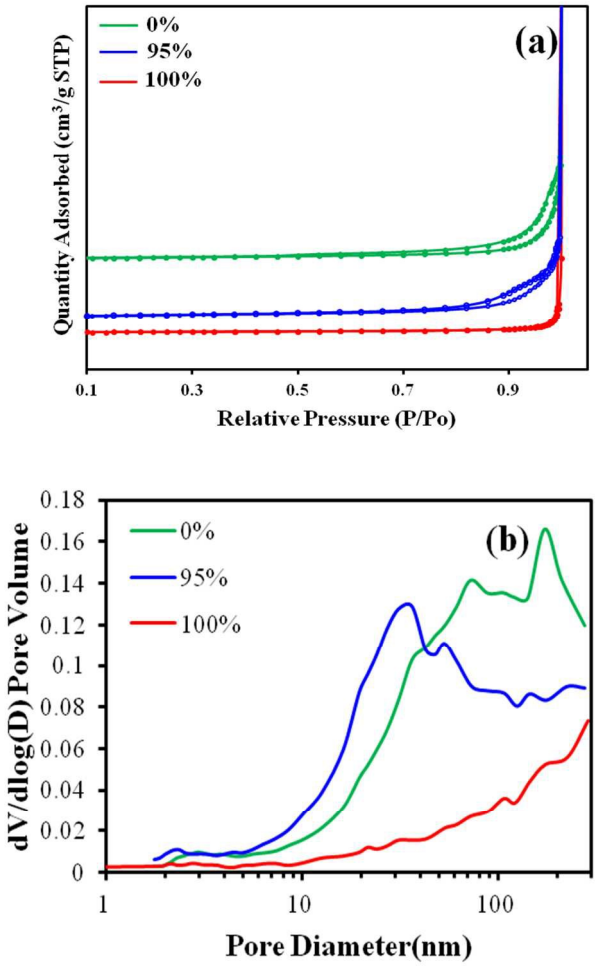


**Figure 10.** (a) $N_2$ adsorption-desorption isotherm and (b) pore size distribution of $Bi_7O_9I_3$/ $Bi_5O_7I$/g-$C_3N_4$ at pH 10.

The durability of the 95wt% $Bi_7O_9I_3/Bi_5O_7I/g\text{-}C_3N_4$ composite is evaluated by recycling the used catalyst. After each cycle, the catalyst is collected by centrifugation. No apparent loss is observed in the photocatalytic activity when CVis removed in the 3rd cycle; even during the fifth run, the decline in the photocatalytic activity is 6% (**Figure 12(a)**). The used 95wt% $Bi_7O_9I_3/Bi_5O_7I/g\text{-}C_3N_4$ composite is also examined by XRD and no detectable difference is observed between the as-prepared and the used samples (**Figure 12(b)**); hence, the 95wt% $Bi_7O_9I_3/Bi_5O_7I/g\text{-}C_3N_4$ composite has good photostability.

As is known, the photocatalysts are excited to generate electron–hole pairs directly after the illumination in the photocatalytic process. Moreover, the photocatalytic efficiency mainly depends on the recombination rate or the lifetime of the photo-generated electron–hole pairs. The faster recombination occurs, the less time is required for the chemical reactions. Therefore, CL spectra are utilized for investigating the recombination rate of the photogenerated electron–hole pairs. To investigate the separation capacity of the photogenerated carriers in the heterostructures, the CL spectra of $g\text{-}C_3N_4$, $Bi_7O_9I_3/Bi_5O_7I$, 50wt% $Bi_7O_9I_3/Bi_5O_7I/g\text{-}C_3N_4$and 90wt% $Bi_7O_9I_3/Bi_5O_7I/g\text{-}C_3N_4$ are measured; the results are shown in **Figure 13(a)**. A strong emission peak around 475 nm appears for the as-prepared samples, which could have been derived from the direct electron–hole recombination of band transitions. However, the characteristic emission peak around the lowest intensity 475 nm for the 90wt% $Bi_7O_9I_3/Bi_5O_7I/g\text{-}C_3N_4$ indicates that the recombination of photogenerated charge carriers is greatly inhibited. The efficient separation of charge could increase the life time of charge carriers and enhance the efficiency of interfacial charge transfer to the adsorbed substrates, thus improving the photocatalytic activity.[16,55] The lowest relative CL intensities of 90wt% $Bi_7O_9I_3/Bi_5O_7I/g\text{-}C_3N_4$ composites, as shown in **Figures 13(a)**, suggest that they possess the lowest recombination rate of electron–hole pairs, resulting in their higher photocatalytic activity, as shown in **Figure 11**. **Figures 13(b)** shows the PL spectra of 90wt% $Bi_7O_9I_3/Bi_5O_7I/g\text{-}C_3N_4$ composites and mechanically mixed $Bi_7O_9I_3/Bi_5O_7I$ with $g\text{-}C_3N_4$samples. The emission intensity of $Bi_7O_9I_3/Bi_5O_7I/g\text{-}C_3N_4$ composites significantly decreases compared with that of the mechanically mixed sample (90%-MM), which indicates that the recombination rate of photogenerated charge carriers is lower in $Bi_7O_9I_3/Bi_5O_7I/g\text{-}C_3N_4$ composites. The PL results confirm the importance of the composites in hindering the recombination of electrons and holesand explain the reason of increasing photocatalytic performance of $Bi_7O_9I_3/Bi_5O_7I/g\text{-}C_3N_4$ composites.

It can be assumed that the enhanced photocatalytic activities of $BiO_xI_y/g\text{-}C_3N_4$ composites could be ascribed to a synergistic effect, including high BET surface area, the formation of the heterojunction, layered structure, and low energy band structure. In the absence of photocatalysts, CV could not be degraded under visible-light irradiation; the superior photocatalytic ability of $BiO_xI_y/g\text{-}C_3N_4$ may be ascribed to its efficient utilization of visible light and high separation efficiency of the electron–hole pairs within its composites.

**Table 4.** Photocatalytic properties of bismuth oxyiodides/$g\text{-}C_3N_4$ nanocomposites photocatalysts under visible light irradiation.

| Composite photocatalyst | Mass fraction of $g\text{-}C_3N_4$ | Parameters of photocatalytic experiments | Photocatalytic activity | Reference Photocatalyst/ photocatalytic activity | Enhancement factor | Reference |
|---|---|---|---|---|---|---|
| $BiOI/g\text{-}C_3N_4$ | 77.5% | Photodegrading methyl blue | 99% decomposition in 3h | $g\text{-}C_3N_4$: 64%<br>BiOI: 51% | 1.5<br>1.9 | 50 |
| $BiOI/g\text{-}C_3N_4$ | 10% | Degradation of bisphenol A | 90.0% decomposition in 3h | $g\text{-}C_3N_4$: 34.0 %<br>BiOI: 78.7% | 3.4<br>1.6 | 51 |
| $BiOI/g\text{-}C_3N_4$ | 15% | rhodamine B, methylene blue, methyl orange, bisphenol A and 4-chlorophenol | 90% decomposition in 30min. | BiOI: 26.3% for rhodamine B | 3.8 | 52 |
| $Bi_5O_7I/g\text{-}C_3N_4$ | 30% | rhodamine B | 90% decomposition in 2h. | $g\text{-}C_3N_4$ : 6.5%<br>$Bi_5O_7I$: 34.5% | 15.3<br>2.9 | 53 |
| $Bi_7O_9I_3/Bi_5O_7I/g\text{-}C_3N_4$ | 5% | crystal violet | 99% decomposition in 24h. | $g\text{-}C_3N_4$ : 25.0%<br>BiOI : 20.0%<br>$Bi_7O_9I_3/Bi_5O_7I$ : 66.7% | 4<br>5<br>1.5 | |

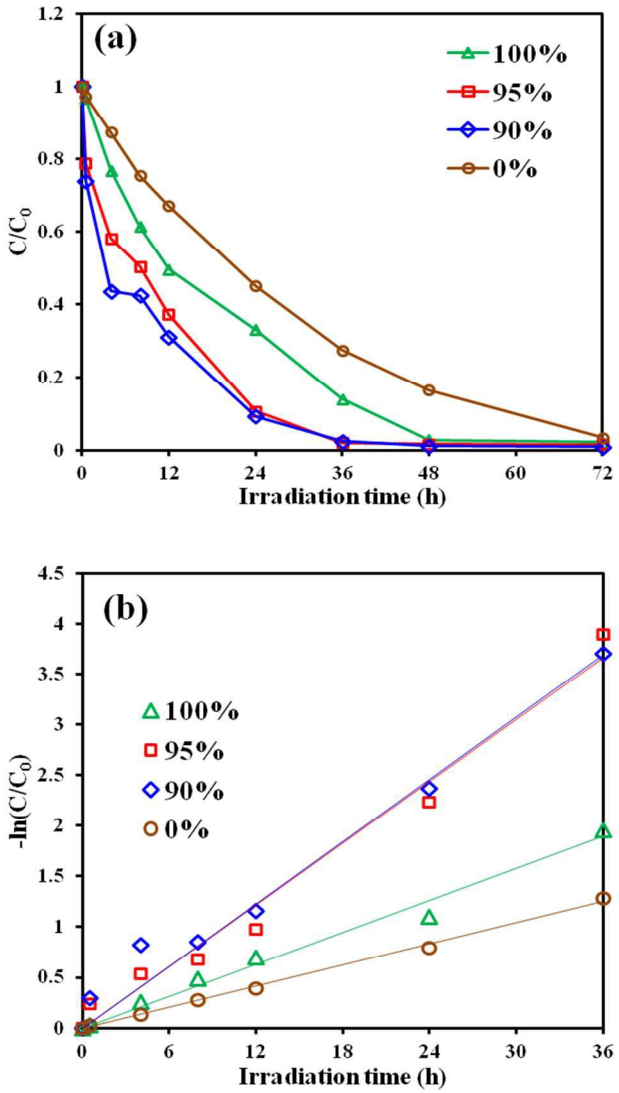


**Figure 11.** Photodegradation of CV as a function ofirradiation time use different $Bi_7O_9I_3/Bi_5O_7I$/g-$C_3N_4$ (pH= 10).

### 3.3 Photodegradation Mechanisms of CV

In general, three possible reaction mechanisms are proposed to be involved in the photodegradation of organics by a semiconductor, including (i) photocatalysis, (ii) photolysis, and (iii) dye photosensitization.[56] In the photolysis process, a photoinduced electron on the induced organics directly reacts with $O_2$ to produce a singlet oxygen atom that acts as an oxidant for the pure organic's photolysis.[57] In the experiments, CV degradation caused by photolysis under visible light in a blank experiment is not observable; CV is a structure-stable dye and the decomposition by the photolysis mechanism is negligible.

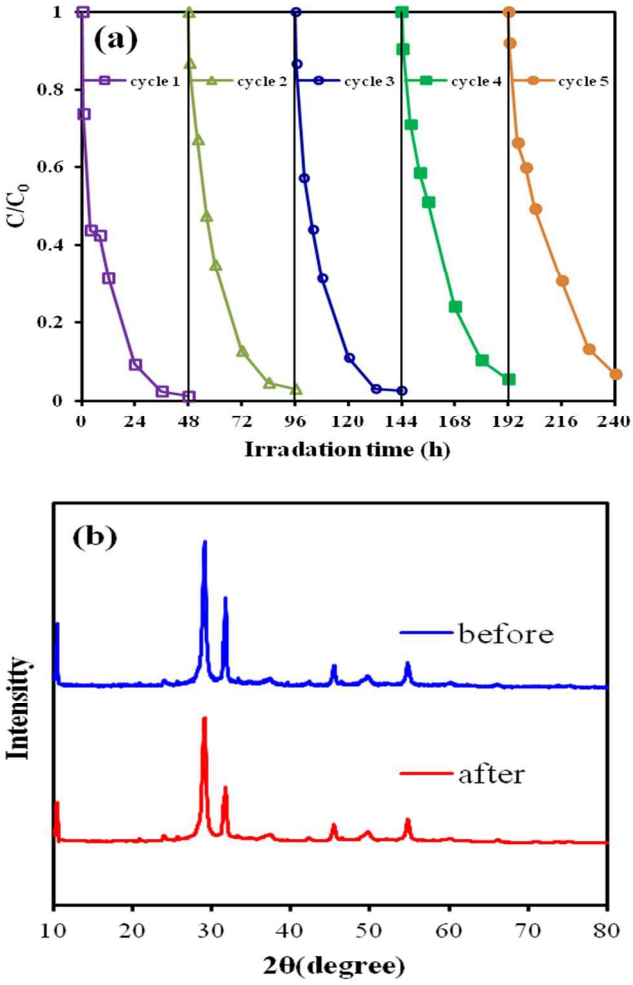


**Figure 12.** (a) Cycling runsin the photocatalytic degradation of CV in the presence of $Bi_7O_9I_3/Bi_5O_7I$/g-$C_3N_4$ (pH=10, 95 wt%), (b) XRD of the sample powder before and after degradation reaction.

As is known to all, various primary reactive species, such as $HO^{\bullet}$, $h^+$, $O_2^{-\bullet}$, $H^{\bullet}$ and $^1O_2$, could be generated during photocatalytic degradation processes in the UV-vis/semiconductor systems.[57,58] Dimitrijevic *et al*. proposed that the water,[58] both dissociated on the surface of $TiO_2$ and in subsequent molecular layers, had a three-fold role of (i) stabilization of charges, preventing electron-hole recombination, (ii) an electron acceptor, the formation of H atoms in a reaction of photo-generated electrons with protons on the surface, $-OH_2^+$, and (iii) an electron donor, the reaction of water with photo-generated holes to give $^{\bullet}OH$ radicals. Di *et al.* revealed that holes werethe main reactive species for the degradation of RhB with g-$C_3N_4$/BiOBr.[59] Chang's group reported by means of active species trapping measurements, revealing that superoxide radicals ($O_2^{-\bullet}$) played a crucial role

during the catalytic process in the Rhodamine B of degradation process using g-$C_3N_4$ nanosheets–BiOCl hybrids.[60] Wang *et al.* reported that •OH radicals were generated by multistep reduction $O_2^{-\bullet}$.[61] The generation of $O_2^{-\bullet}$ could not only inhibit the recombination of photoinduced charge carriers, but also benefit the de-chlorination of chlorinated phenol derivative. The hydroxyl radical HO$^\bullet$ might only be formatted via an $e^- \rightarrow O_2^{-\bullet} \rightarrow H_2O_2 \rightarrow {}^\bullet OH$ route. Meanwhile, $^\bullet$OH radicalswere formatted by multistep reduction $O_2^{-\bullet}$ in the system.[62] Zhu *et al.* reported that the g-$C_3N_4$/BiOBr-mediated photodegradation of methylene blue molecules was mainly attributed to the oxidation action of the generated $O_2^{-\bullet}$ radicals and partly to the action of $h^+$ via direct hole oxidation process.[63] According to earlier studies, the photocatalytic process was mainly governed by $O_2^{-\bullet}$, rather than by $^\bullet$OH, $e^-$ or $h^+$.[60] In earlier study, CV photodegradation by $BiO_mX_n/BiO_pX_q$ (X,Y=Cl, Br, I) under visible light was dominated by $O_2^{-\bullet}$ oxidation being the main active species and $^\bullet$OH and $h^+$ being the minor active species.[42,55] On the basis of the references presented above, it is proposed that the probability of forming $^\bullet$OH should be much lower than that for $O_2^{-\bullet}$; however, $^\bullet$OH is an extremely strong and nonselective oxidant, which leads to the partial or complete mineralization of several organic chemicals.

From **Figure 14(a)-(b)**, not only the six characteristic peaks (strong) of the DMPO-$O_2^{-\bullet}$ adducts are observed, but also the four characteristic peaks (weak) of DMPO-$^\bullet$OH adducts (1:2:2:1 quartet pattern) are observed under visible light irradiated 95wt% $Bi_7O_9I_3/Bi_5O_7I$/g-$C_3N_4$ composites dispersion. **Figure 14(a)(b)** indicates that no EPR signal is observed when the reaction is performed in the dark, while the signals with intensity corresponding to the characteristic peak of DMPO-$^\bullet$OH and DMPO-$O_2^{-\bullet}$ adducts[25] are observed during the reaction process under visible light irradiation, and the intensity gradually increases with the prolonged reaction time, suggesting that $O_2^{\bullet-}$ as major and $^\bullet$OH as minor active species are formed in the presence of 95wt% $Bi_7O_9I_3/Bi_5O_7I$/g-$C_3N_4$ composites and oxygen under visible light irradiation.

In order to re-evaluate the effect of the active species during the photocatalytic reaction, a series of quenchers are introduced to scavenge the relevant active species. As shown in **Figure 14(c)**, the photocatalytic degradation of CV is not affected by the addition of IPA, while the degradation efficiency of BQ and AO quenching decreases evidently compared with that of no-quenching, whereas $O_2^{\bullet-}$ are the major and $h^+$ and $^\bullet$OH minor active species in the process of photocatalytic degradation for CV. Therefore, the quenching effects of different scavengers and EPR display that the reactive $O_2^{\bullet-}$ plays the major role and $^\bullet$OH plays the minor role in the CV of the photocatalytic degradation.

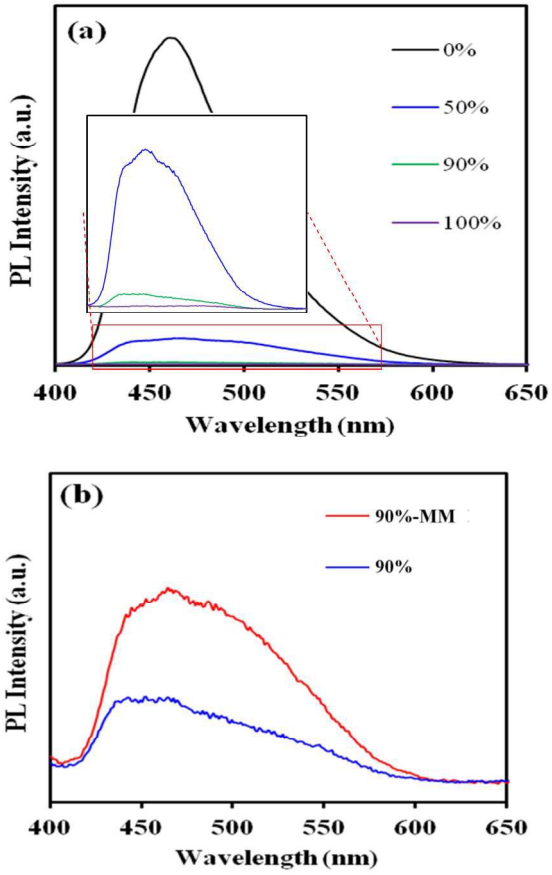


**Figure 13.** (a) PL spectrum of $Bi_7O_9I_3/Bi_5O_7I$/g-$C_3N_4$ samples under pH 10, and (b) Mechanical Mixing and hydrothermal method compare.

Fan *et al.* reported that Pt-$TiO_2$ gathered less negative species on catalyst surfaces, which deteriorated reaction rates, than pure $TiO_2$ did in an acidic environment.[64] The $^\bullet$OH radical is subsequently produced. The $^\bullet$OH radical is produced subsequently, as also shown in eqs.8-13.

$$O_2^{-\bullet} + H^+ + e^- \rightarrow HOO^\bullet \quad (8)$$

$$HOO^\bullet + H_2O \rightarrow {}^\bullet OH + H_2O_2 \quad (9)$$

$$O_2^{-\bullet} + 2H^+ \rightarrow H_2O_2 \quad (10)$$

$$H_2O_2 + e^- \rightarrow {}^\bullet OH + OH^- \quad (11)$$

$$h^+ + OH^- \rightarrow {}^\bullet OH \quad (12)$$

$$h^+ + H_2O \rightarrow {}^\bullet OH + H^+ \quad (13)$$

On the basis of above experimental results, a detailed mechanism of degradation is illustrated in **Figure 15.** Once

the electron reaches the conduction band of $BiO_xI_y$, it induces the formation of active oxygen species, which cause the degradation of CV dye. It is clear that, except for the photodegradation of CV by the route of $BiO_xI_y$/g-$C_3N_4$-mediated and photosensitized processes, another type of photocatalytic route accounts for the enhanced photocatalytic activity. Both the photosensitized and photocatalytic processes are preceded concurrently (**Figure 15**). However, in photosensitized and photocatalytic reaction conditions, $O_2^{\bullet-}$ radicalsare generated by the reaction of photogenerated and photosensitized electron with oxygen gas on the photocatalyst surface, and $^{\bullet}OH$ radicalsare also generated by the reaction of $O_2^{\bullet-}$ radicals with $H^+$ ion and hole $h^+$ with $OH^-$ ion (or $H_2O$). The $^{\bullet}OH$ radical is produced subsequently, as expressed in Eqs. (8) to (13). These cycles continuously happen when the system is exposed to visible-light irradiation;[57] and, after several cycles of photo-oxidation, the degradation of CV by the generated oxidant species can be expressed by Eqs. 14-15:

$$CV + OH^{\bullet} / O_2^{-\bullet} \rightarrow \text{degraded compounds} \quad (14)$$

$$CV^{+\bullet} + OH^{\bullet} / O_2^{-\bullet} \rightarrow \text{degraded compounds} \quad (15)$$

In visible light-induced semiconductor system, hydroxylated compounds were also identified for the photocatalytic degradation of CV.[42,55] In earlier reports,[64,65] the *N*-dealkylation processes were preceded by the formation of a nitrogen-centered radical, and the oxidative degradation (destruction of the dye chromophore structure) was preceded by the generation of a carbon-centered radical in the photocatalytic degradation of CV dye under UV light irradiation. All the intermediates identified in these two studied topics had the same results under visible or UV light irradiation. It was doubtless that the major oxidant was $^{\bullet}OH$ radicals, not $O_2^{-\bullet}$ radicals. The reaction mechanisms for $BiO_xI_y$/g-$C_3N_4$-mediated photocatalytic processes proposed in this research should offer some notion for the applications to the decoloration of dyes.

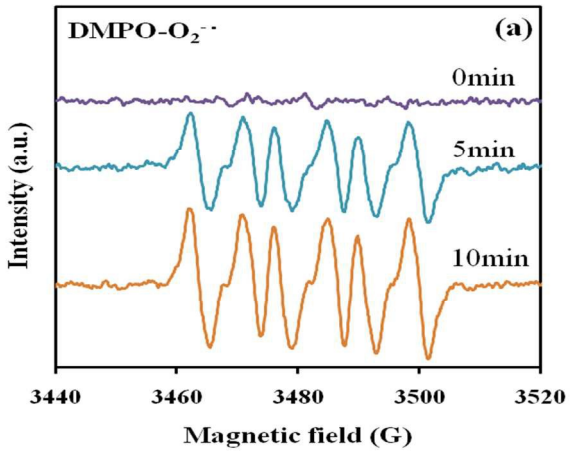


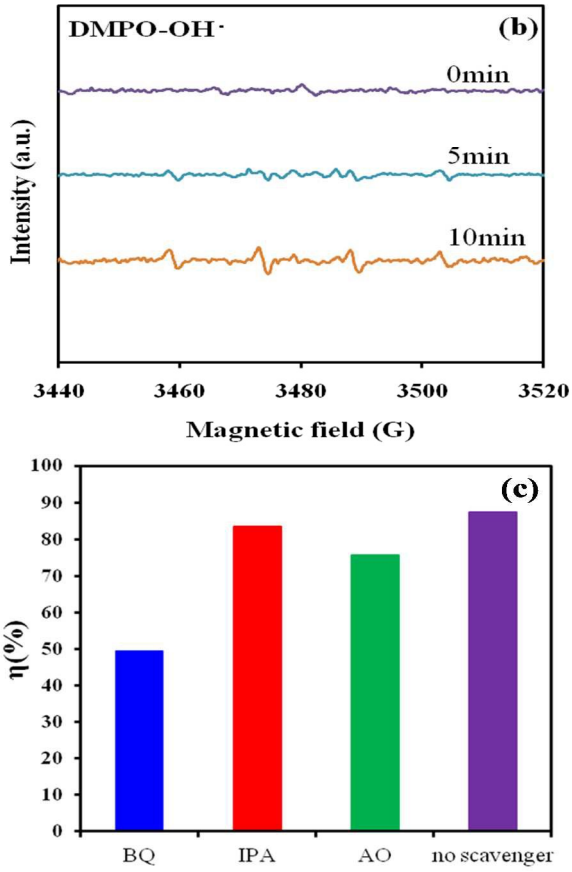


**Figure 14.** (a) (b) DMPO spin trapping EPR spectra for DMPO–$O_2^{\bullet-}$ and DMPO–$^{\bullet}OH$ under visible light irradiation with $Bi_7O_9I_3$/$Bi_5O_7I$/g-$C_3N_4$ (pH=10, 95wt%) photocatalyst. (c) The dye concentration during photodegradation as a function of irradiation time observed in $Bi_7O_9I_3$/$Bi_5O_7I$/g-$C_3N_4$ photocatalyst under the addition of different scavengers of IPA, AQ, and BQ.

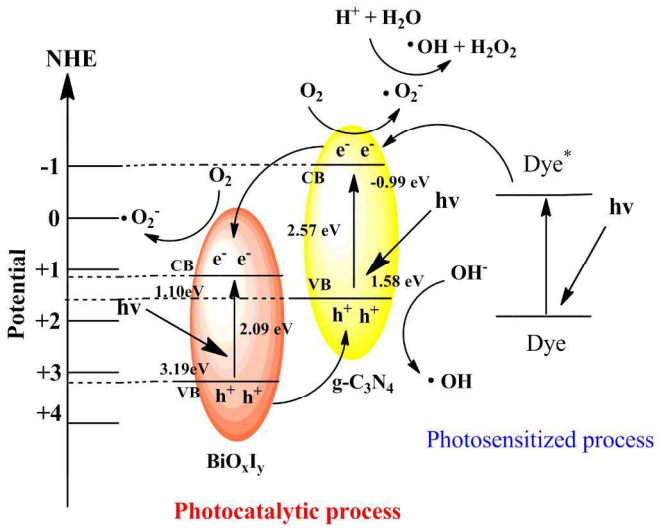


**Figure 15.** The band structure diagram of $Bi_5O_7I$/g-$C_3N_4$ and the possible charge separation processes.

# 4. Conclusions

The novel composites of $BiO_xI_y$/g-$C_3N_4$ are prepared by hydrothermal method. This is the first report to demonstrate the controlled synthesis of a series of $BiO_xI_y$/g-$C_3N_4$composites. The removal efficiency is significantly enhanced in the presence of 95wt% $Bi_7O_9I_3$/$Bi_5O_7I$/g-$C_3N_4$.The increased photocatalytic activities of $BiO_xI_y$/g-$C_3N_4$ could be attributed to the formation of the heterojunction between $BiO_xI_y$ and g-$C_3N_4$, which effectively suppresses the recombination of photo-induced electron–hole pairs.It can be assumed that the enhanced photocatalytic activities of $BiO_xI_y$/g-$C_3N_4$ materials could be ascribed to the formation of the heterojunction.$O_2^{-\bullet}$ is major and$h^+$and$^\bullet$OH is minor active species in the photocatalytic process. In particular, the heterojunction systems $BiO_xI_y$/g-$C_3N_4$ exhibit high catalytic activity and stability, performing as authentic heterogeneous visible-light-driven photocatalysts to degrade organic pollutants efficiently.

## Acknowledgements

This research was supported by the Ministry of Science and Technology of the Republic of China (MOST-104-2113-M-142-001).

## Notes and references

1 D.F. Duxbury, The photochemistry and photophysics of triphenylmethane dyes in solid and liquid media, *Chem. Rev.*, 1993, **93**, 381-433.

2 T. Inoue , K. Kikuchi, K. Hirose, M. Iiono and T. Nagano, Small molecule-based laser inactivation of inositol 1,4,5-trisphosphate receptor, *Chem. Biol.*, 2001, **8**, 9-15.

3 R. Bonnett and G. Martinez,Photobleaching of sensitisers used in photodynamic therapy, *Tetrahedron*, 2001, **57**, 9513-9547.

4 B. P. Cho, T. Yang, L. R. Blankenship, J. D. Moody, M. Churchwell, F. A. Bebland and S. J. Culp, Synthesis and Characterization of *N*-Demethylated Metabolites of Malachite Green and Leucomalachite Green, *Chem. Res. Toxicol.*, 2003, **16**, 285-294.

5 A. Kubacka, M. Fernández-García, and G. Colón, Advanced Nanoarchitectures for Solar Photocatalytic Applications, *Chem. Rev.*, 2012, **112**, 1555–1614.

6 K. Kalantar-zadeh, J.Z. Ou, T. Daeneke, M.S. Strano, M.Pumera and S.L. Gras, Two-Dimensional Transition Metal Dichalcogenides in Biosystems, *Adv. Funct. Mater.,* 2015, **25**, 5086–5099.

7 W. Zhang, B.S. Naidu, J.Z. Ou, A.P. O'Mullane, A.F. Chrimes, B.J. Carey, Y. Wang, S.Y. Tang, V. Sivan, A. Mitchell, S.K. Bhargava and K. Kalantar-zadeh, Liquid Metal/Metal Oxide Frameworks with Incorporated $Ga_2O_3$ for Photocatalysis, *ACS Appl. Mater. Interfaces*, 2015, **7**, 1943−1948

8 W. Zhang, J.Z. Ou, S.Y. Tang, V. Sivan, D.D. Yao, K. Latham, K. Khoshmanesh, A. Mitchell, A.P. O'Mullane and K. Kalantar-zadeh, Liquid Metal/Metal Oxide Frameworks, *Adv. Funct. Mater.,* 2014, **24**, 3799-3807.

9 W. W. Lee, C. S. Lu, C. W. Chuang, Y. J. Chen, J. Y. Fu, C. W. Siao and C. C. Chen, Synthesis of bismuth oxyiodides and their composites: characterization, photocatalytic activity, and degradation mechanisms, *RSC Adv.*, **5**, 2015, 23450–23463

10 K. Yu, S. Yang, C. Liu, H. Chen, H. Li, C. Sun and S.A. Boyd, *Environ. Sci. Technol.*, 2012, **46**, 7318−7326.

11 W.L.W. Lee, J.S. Lin, J.L. Chang, J.Y. Chen, M.C. Cheng and C.C. Chen, Photodegradation of CV over nanocrystalline bismuth tungstate prepared by hydrothermal synthesis, *J. Mol. Catal. A: Chem.*, 2012, **361–362**, 80–90.

12 F. Chen, P. Fang, Y. Gao, Z. Liu, Y. Liu and Y. Dai, Effective removal of high-chroma crystal violet over $TiO_2$-based nanosheet by adsorption–photocatalytic degradation, *Chem. Eng. J.*, 2012, **204–206**, 107–113.

13 S. Ameen, M.S. Akhtar, M. Nazim and H.S. Shin, Rapid photocatalytic degradation of crystal violet dye over ZnO flower nanomaterials, *Mater. Lett.*, 2013, **96**, 228–232.

14 W.L. W. Lee, W.H. Chung, W.S. Huang, W.C. Lin, W.Y. Lin, Y.R. Jiang and C.C. Chen, Photocatalytic activity and mechanism of nano-cubic barium titanate prepared by a hydrothermal method, *J. Taiwan Inst. Chem. Eng.*, 2013, **44**, 660–669.

15 W. Wang, M. O. Tadé and Z. Shao, Research progress of perovskite materials in photocatalysis- and photovoltaics-related energy conversion and environmental treatment, *Chem. Soc. Rev.*, 2015,**44**, 5371-5408

16 Y.R. Jiang, H.P. Lin, W.H. Chung, Y.M. Dai, W.Y. Lin, C.C. Chen, Controlled hydrothermal synthesis of $BiO_xCl_y$/$BiO_mI_n$ composites exhibiting visible-light photocatalytic degradation of crystal violet, *J. Hazard. Mat.*,2015, **283**, 787-805.

17 T. Li, L. Zhao, Y. He, J. Cai, M. Luo, J. Lin, Synthesis of g-$C_3N_4$/$SmVO_4$ composite photocatalyst with improved visible light photocatalytic activities in RhB degradation, *Appl. Catal. B: Environ.*,2013, **129**, 255-263.

18 H. Cheng, B. Huang and Y. Dai, Engineering BiOX (X = Cl, Br, I) nanostructures for highly efficient photocatalytic applications, *Nanoscale*, 2014, **6**, 2009-2026.



 

19 X. Xiao and W.D. Zhang, Facile synthesis of nanostructured BiOI microspheres with high visible light-induced photocatalytic activity, *J. Mater. Chem.*, 2010, **20**, 5866–5870.
20 Jie Li, Ying Yu and Lizhi Zhang, Bismuth oxyhalide nanomaterials: layered structures meet photocatalysis, *Nanoscale*, 2014, **6**, 8473-8488.
21 Y. Huo, J. Zhang, M. Miao and Y. Jin, Solvothermal synthesis of flower-like BiOBr microspheres with highly visible-light photocatalytic performances, *Appl. Catal. B: Environ.*, 2012, **111-112**, 334-341.
22 Q.C. Liu, D.K. Ma, Y.Y. Hu, Y.W. Zeng and S.M. Huang,Various Bismuth Oxyiodide Hierarchical Architectures: Alcohothermal-Controlled Synthesis, Photocatalytic Activities, and Adsorption Capabilities for Phosphate in Water, *ACS Appl. Mater. Interfaces*, 2013, **5**, 11927–11934.
23 L. Ye, J. Chen, L. Tian, J. Liu, T. Penga, K. Deng and L. Zan,BiOI thin film via chemical vapor transport: Photocatalytic activity, durability, selectivity and mechanism, *Appl. Catal. B: Environ.*, 2013, **130– 131**, 1– 7.
24 X. Chang, J. Huang, C. Cheng, Q. Sui, W. Sha, G. Ji, S. Deng and G. Yu, BiOX (X = Cl, Br, I) photocatalysts prepared using $NaBiO_3$ as the Bi source: Characterization and catalytic performance, *Catal. Commun.*, 2010, **11**, 460–464.
25 X. Xiao, C. Xing, G. He, X. Zuo, J. Nan and L. Wang, Solvothermal synthesis of novel hierarchical $Bi_4O_5I_2$ nanoflakes with highly visible light photocatalytic performance for the degradation of 4-tert-butylphenol, *Appl. Catal. B: Environ.,* 2014, **148–149**, 154–163.
26 X. Xiao, R. Hao, X. Zuo, J. Nan, L. Li and W. Zhang,Microwave-assisted synthesis of hierarchical $Bi_7O_9I_3$ microsheets for efficient photocatalytic degradation of bisphenol-A under visible light irradiation, *Chem. Eng. J.*, 2012, **209**, 293–300.
27 W.L. Huang and Q.S. Zhu,DFT calculations on the electronic structures of BiOX (X = F, Cl, Br, I) photocatalysts with and without semicore Bi 5d states, *J. Comput. Chem.*, 2009, **30**, 183–190.
28 X. Xiao, C. Liu, R. Hu, X. Zuo, J. Nan, L. Li and L. Wang, Oxygen-rich bismuth oxyhalides: generalized one-pot synthesis, band structures and visible-light photocatalytic properties, *J. Mater. Chem.*, 2012, **22**, 22840–22843.
29 X. Xiao, R. Hu, C. Liu, C. Xing, C. Qian, X. Zuo, J. Nan and L. Wang,Facile large-scale synthesis of β-$Bi_2O_3$ nanospheres as a highly efficient photocatalyst for the degradation of acetaminophen under visible light irradiation, *Appl. Catal. B: Environ.*, 2013, **140–141**, 433–443.
30 Z. Zhao, Y. Sun and F. Dong, Graphitic carbon nitride based nanocomposites: a review, *Nanoscale*, 2015, **7**, 15-37.
31 X. Wang, Q. Wang, F. Li , W. Yang, Y. Zhao, Y. Hao and S. Liu, Novel BiOCl–$C_3N_4$ heterojunction photocatalysts: In situ preparation via an ionic-liquid-assisted solvent-thermal route and their visible-light photocatalytic activities, *Chem. Enginer. J.*, 2013, **234**, 361–371.
32 L. Ye, J. Liu, Z. Jiang, T. Peng and L. Zan, Facets coupling of BiOBr-g-$C_3N_4$ composite photocatalyst forenhanced visible-light-driven photocatalytic activity, *Appl. Catal. B: Environ.*,2013, **142–143**, 1– 7.
33 J. Di, J. Xia, S. Yin, H. Xu, L. Xu, Y. Xu, M. He and H. Li, Preparation of sphere-like g-$C_3N_4$/BiOI photocatalysts via a reactable ionic liquid for visible-light-driven photocatalytic degradation of pollutants, *J. Mater. Chem. A*, 2014, **2**, 5340–5351.
34 C. Chang, L. Zhu, S. Wang, X. Chu and L. Yue,Novel Mesoporous Graphite Carbon Nitride/BiOI Heterojunction for Enhancing Photocatalytic Performance Under Visible-Light Irradiation, *ACS Appl. Mater. Interfaces*, 2014, **6**, 5083−5093.
35 H. Liu, Y. Su, Z. Chen, Z.Jin and Y. Wang, Graphene sheets grafted three-dimensional $BiOBr_{0.2}I_{0.8}$ microspheres with excellent photocatalytic activity under visible light, *J. Hazard. Mater.*,2014, **266**, 75– 83.
36 B.P. Barbero and L.E. Cadus, $V_2O_5$–$SmVO_4$ mechanical mixture: oxidative dehydrogenation of propane, *Appl. Catal. A*, 2002, **237**, 263–273.
37 M.C. Yin, Z.S. Li, J.H. Kou and Z.G. Zou, Mechanism Investigation of Visible Light-Induced Degradation in a Heterogeneous $TiO_2$/Eosin Y/Rhodamine B System, *Environ. Sci. Technol.*,2009, **43**, 8361-8366.
38 L.S. Zhang, K.H. Wong, H.Y. Yip, C. Hu, J.C. Yu, C.Y. Chan and P.K. Wong, Effective Photocatalytic Disinfection of E. coli K-12 Using AgBr-$AgBi_2$-$WO_6$ Nanojunction System Irradiated by Visible Light: The Role of Diffusing Hydroxyl Radicals, *Environ. Sci. Technol.*,2010, **44**, 1392-1398.
39 S.G. Meng, D.Z. Li, M. Sun, W.J. Li, J.X. Wang, J. Chen, X.Z. Fu and G.C. Xiao,Sonochemical synthesis, characterization and photocatalytic properties of a novel cube-shaped $CaSn(OH)_6$, *Catal. Commun.*,2011, **12**, 972-975.
40 G. Li, K.H. Wong, X. Zhang, C. Hu, J.C. Yu, R.C.Y. Chan and P.K. Wong,Degradation of Acid Orange 7 using magnetic AgBr under visible light: The roles of oxidizing species, *Chemosphere*, 2009,**76**, 1185-1191.
41 X. Xiao and W.D. Zhang, Hierarchical $Bi_7O_9I_3$ micro/nano-architecture: facile synthesis, growth

mechanism, and high visible light photocatalytic performance, *RSC Adv.*, 2011, **1**, 1099–1105.
42 S.T. Huang, Y.R. Jiang, S.Y. Chou, Y.M. Dai and C.C. Chen, Synthesis, characterization, photocatalytic activity of visible-light-responsive photocatalysts $BiO_xCl_y/BiO_mBr_n$ by controlled hydrothermal method, *J. Mol. Catal. A: Chem.*, 2014, **391**, 105–120.
43 S. C. Yan, Z. S. Li and Z.G. Zou, Photodegradation Performance of g-$C_3N_4$ Fabricated by Directly Heating Melamine, *Langmuir*, 2009, **25**, 10397–10401.
44 J. Zhang, M. Zhang, G. Zhang and X. Wang, Synthesis of Carbon Nitride Semiconductors in Sulfur Flux for WaterPhotoredox Catalysis, *ACS Catal.*, 2012,**2**, 940−948.
45 Y.H. Liao, J.X. Wang, J.S. Lin, W.H. Chung, W.Y. Lin and C.C. Chen,Synthesis photocatalytic activities and degradation mechanism of $Bi_2WO_6$ toward crystal violet dye, *Catal. Today*, 2011, **174**, 148-159.
46 Y. Li, H. Zhang, P. Liu, D. Wang, Y. Li and H. Zhao,Cross-Linked g-$C_3N_4$/rGO Nanocomposites with Tunable Band Structure and Enhanced Visible Light Photocatalytic Activity, *Small*,2013, **9**, 3336−3344.
47 M. Xu, L. Han and S. Dong,Facile Fabrication of Highly Efficient g-$C_3N_4$/$Ag_2O$ Heterostructured Photocatalysts with Enhanced Visible-Light Photocatalytic Activity, *ACS Appl. Mater. Interfaces*, 2013, **5**, 12533–12540.
48 L. Lin, S. Yuan, J. Chen, L. Wang, J. Wan and X. Lu, Treatment of chloramphenicol-contaminated soil by microwave radiation, *Chemosphere*,2010,**78**, 66–71.
49 A. Chatzitakis, C. Berberidou, I. Paspaltsis, G. Kyriakou, T. Sklaviadis, and I. Poulios,Photocatalytic degradation and drug activity reduction of Chloramphenicol, *Water Res.*, 2008, **42**, 386-394.
50 D. L. Jiang, L. l. Chen, J. J. Zhu, M. Chen, W. D. Shi and J. M. Xie, *Dalton Trans.*, 2013, **42**, 15726–15734.
51 C. Chang, L. Zhu, S. Wang, X. Chu and L. Yue, *ACS Appl. Mater. Interfaces*, 2014, **6**, 5083−5093.
52 J. Di, J. Xia, S. Yin, H. Xu, L. Xu, Y. Xu, M. Hea and H. Li, *J. Mater. Chem. A*, 2014, **2**, 5340–5351.
53 C. Liu, H. Huang, X. Du, T. Zhang, N. Tian, Y. Guo, and Y. Zhang, *J. Phys. Chem. C,* 2015, **119**, 17156−17165.
54 Z. Zhao, Y. Sun and F. Dong, Graphitic carbon nitride based nanocomposites: a review, *Nanoscale*, **2015**, 7, 15-37.
55 Y. R. Jiang, S. Y. Chou, J. Lin Chang, S. T. Huang, H. P. Lin, C. C. Chen, Hydrothermal Synthesis of Bismuth Oxybromide-BismuthOxyiodide Composites with highly visible light Photocatalyticperformance for the degradation of CV and Phenol, *RSC Advances*, **2015**, 5, 30851-30860
56 C. Nasr, K. Vinodgopal, L. Fisher, S. Hotchandani, A. K. Chattopadhyay and P. V. Kamat,Environmental Photochemistry on Semiconductor Surfaces. Visible Light Induced Degradation of a Textile Diazo Dye, Naphthol Blue Black, on $TiO_2$ Nanoparticles, *J. Phys. Chem.*,1996, **100**, 8436–8442.
57 X. Xiao, R. Hao, M. Liang, X. Zuo, J. Nan, L. Li and W. Zhang, One-pot solvothermal synthesis of three-dimensional (3D) BiOI/BiOCl composites with enhanced visible-light photocatalytic activities for the degradation of bisphenol-A, *J. Hazard. Mater.,*2012, **233–234**, 122–130.
58 N.M. Dimitrijevic, B.K. Vijayan, O.G. Poluektov, T. Rajh, K.A. Gray, H. He and P. Zapol,Role of Water and Carbonates in Photocatalytic Transformation of $CO_2$ to $CH_4$ on Titania, *J. Am. Chem. Soc.*,2011, **133**, 3964-3971.
59 J. Di, J. Xia, S. Yin, H. Xu, M. He, H. Li, L. Xu and Y. Jiang, A g-$C_3N_4$/BiOBr visible-light-driven composite: synthesis via a reactable ionic liquid and improved photocatalytic activity, *RSC Adv.*, 2013, **3**, 19624–19631
60 H. Li, J. Liu, W. Hou, N. Du, R. Zhang and X. Tao, Synthesis and characterization of g-$C_3N_4$/$Bi_2MoO_6$ heterojunctions with enhanced visible light photocatalytic activity, *Appl. Catal. B: Environ.*,2014, **160–161**, 89–97.
61 S. Shenawi-Khalil, V. Uvarov, S. Fronton, I. Popov and Y. Sasson,A Novel Heterojunction BiOBr/Bismuth Oxyhydrate Photocatalyst with Highly Enhanced Visible Light Photocatalytic Properties, *J. Phys. Chem. C*, 2012, **116**, 11004−11012.
62 Y.Tian, B.Chang, J.Lu, J.Fu, F.Xi and X.Dong, Hydrothermal Synthesis of Graphitic Carbon Nitride–$Bi_2WO_6$ Heterojunctions with Enhanced Visible Light Photocatalytic Activities,*ACS Appl. Mater. Interfaces*, 2013, **5**, 7079–7085.
63 D. Jiang, L. Chen, J. Zhu, M. Chen, W. Shi and J. Xie, Novel p–n heterojunction photocatalyst constructed by porous graphite-like $C_3N_4$ and nanostructured BiOI: facile synthesis and enhanced photocatalytic activity, *Dalton Trans.*, 2013, **42**, 15726.
64 H. J. Fan, C. S. Lu, W. L. W. Lee, M. R. Chiou and C. C. Chen,Mechanistic pathways differences between P25-$TiO_2$ and Pt-$TiO_2$ mediated CV photodegradation, *J. Hazard. Mater.* 2011, **185**, 227–235.
65 H. L. Chen, W. W. Lee, W. H. Chung, Y. J. Chen, Y. R. Jiang, H. P. Lin, W. Y. Lin, C. C. Chen, Controlled Hydrothermal Synthesis of Bismuth



 

Oxybromides and Their Photocatalytic Properties, *J. Taiwan Inst. Chem. Eng.*2013, **44**, 660–669.